JOURNAL OF SPACECRAFT AND ROCKETS
Vol. 38, No. 5, September–October 2001

X-33 Experimental Aeroheating at Mach 6 Using Phosphor Thermography

Thomas J. Horvath,* Scott A. Berry,* Brian R. Hollis,† Derek S. Liechty,* H. Harris Hamilton II,† and N. Ronald Merski†
NASA Langley Research Center, Hampton, Virginia 23681

The goal of the NASA reusable launch vehicle technology program is to mature and demonstrate essential, cost-effective technologies for next-generation launch systems. The X-33 flight vehicle presently being developed by Lockheed Martin is an experimental single-stage-to-orbit demonstrator that seeks to validate critical technologies and ensure applicability to a full-scale reusable launch vehicle. As with the design of any hypersonic vehicle, the aeroheating environment is an important issue, and one of the key technologies being demonstrated on X-33 is an advanced metallic thermal protection system. As part of the development of this thermal protection system, the X-33 aeroheating environment is being defined through conceptual analysis, ground-based testing, and computational fluid dynamics. An overview of the hypersonic aeroheating wind-tunnel program conducted at the NASA Langley Research Center in support of the ground-based testing activities is provided. Global surface heat transfer images, surface streamline patterns, and shock shapes were measured on 0.013 scale (10-in.) ceramic models of the proposed X-33 configuration in Mach 6 air. The test parametrics include angles of attack from −5 to 40 deg, unit Reynolds numbers from 1×10^6 to 8×10^6/ft, and body-flap deflections of 0, 10, and 20 deg. Experimental and computational results indicate the presence of shock/shock interactions that produced localized heating on the deflected flaps and boundary-layer transition on the canted fins. Comparisons of the experimental data to laminar and turbulent predictions were performed. Laminar windward heating data from the wind tunnel was extrapolated to flight surface temperatures and generally compared to within 50°F of flight prediction along the centerline. When coupled with the phosphor technique, this rapid extrapolation method would serve as an invaluable thermal protection system design tool.

Nomenclature

H	=	enthalpy, Btu/lbm
h	=	heat transfer coefficient, $\dot{q}/(H_{aw} - H_w)$, where $H_{aw} = H_{t,2}$, lbm/(ft^2 · s)
M	=	Mach number
P	=	pressure, psia
$\dot{q}$	=	heat transfer rate, Btu/(ft^2·s)
Re	=	unit Reynolds number, 1/ft
r	=	radius, in.
T	=	temperature, °R
t	=	time, s
u	=	velocity, ft/s
x	=	axial distance from origin, in.
y	=	lateral distance from origin, in.
z	=	vertical distance from origin, in.
α	=	angle of attack, deg
δ	=	control surface deflection, deg

Subscripts

aw	=	adiabatic wall
BF	=	body flap
b	=	reference span
FR	=	Fay–Riddell, stagnation-point, reference heating condition
L	=	reference length
n	=	model nose
$t, 1$	=	reservoir conditions
$t, 2$	=	stagnation conditions behind normal shock
w	=	wall
∞	=	freestream conditions

Received 23 July 1999; revision received 7 November 1999; accepted for publication 7 February 2001.

*Aerospace Technologist, Aerothermodynamics Branch, Aerodynamics, Aerothermodynamics, and Acoustics Competency.

†Aerospace Technologist, Aerothermodynamics Branch, Aerodynamics, Aerothermodynamics, and Acoustics Competency. Member AIAA.

Introduction

THE access to space study[1] conducted by NASA recommended the development of a fully reusable launch vehicle (RLV)[2–4] to provide a next-generation launch capability at greatly reduced cost. This led to the RLV/X-33 technology program, an industry-led effort in partnership with NASA. The primary goal of the RLV/X-33 technology program is to enable significant reductions in the cost of access to space. The full-scale RLV system must be lightweight enough to achieve orbit and deliver a payload in a cost-effective manner. As part of the RLV program, the X-33 is envisioned as a subscale rocket technology demonstrator for a single-stage-to-orbit (SSTO) RLV. The proposed X-33 vehicle is intended to demonstrate key design and operational aspects of a commercially viable system SSTO RLV rocket. Following a Phase I industry competition for X-33, Lockheed Martin's lifting body concept was selected by NASA and Lockheed was awarded a Phase II contract (July 1996) to pursue construction of the flight vehicle. Lockheed's current lifting body design (Fig. 1), shown in the dimensioned sketch at model scale, represents a one-half scale RLV. It incorporates symmetric canted fins, twin vertical tails, and two body flaps located at the rear of the fuselage for aerodynamic control, and it is powered by a linear aerospike engine.[5]

As part of the industry/government partnership, NASA Langley Research Center (LaRC) has been tasked with providing aerodynamic and surface heating data, including transition criteria, to Lockheed Martin in support of X-33 development and design. To meet the aerothermodynamic objectives outlined in the resulting tasks, a synergistic experimental/computational approach was utilized. A synoptic of the testing, computational, and analysis capabilities performed at NASA LaRC as applied to X-33 is provided in Ref. 6. Results from early Phase II wind-tunnel heating measurements were compared to laminar and turbulent computational fluid dynamics (CFD) computations.[7] Flight peak heating rates over the X-33 were then predicted with both an engineering code and a Navier–Stokes solver. The early data set was also used to formulate and support the use of a Re_θ/M_e criteria to predict transition onset

Table 1 X-33 phase 2 aeroheating tests in NASA LaRC Aerothermodynamics Branch tunnels

Year	Tunnel	Test	Occupancy dates	Runs	Description
1996	20-in. M6	6731	Aug. 28–Sept. 13	1–46	D-loft forebody baseline
1996	M6 CF4	114	Oct. 17–Nov. 6	1–43	Yaw dispersions
1996	20-in. M6	6737	Dec. 6–Dec. 20	1–174	D-loft forebody transition
1997	20-in. M6	6751	June 23–June 30	1–52	Generic bowed-panel models
1997	20-in. M6	6751	July 15–July 17	52–56	Generic bowed-panel models
1997	20-in. M6	6753	July 17–July 22	1–22	Rev-C (37-deg dihedral) baseline
1997	20-in. M6	6753	Aug. 12–Aug. 20	22–50	Rev-C (37-deg dihedral) baseline
1997	20-in. M6	6751	Aug. 27–Aug. 29	56–99	Generic bowed-panel models
1997	20-in. M6	6751	Sept. 22–Sept. 24	100–115	Generic bowed-panel models
1997	20-in. M6	6763	Dec. 30–Jan. 6	1–29	Rev-F (20-deg dihedral) baseline
1998	20-in. M6	6763	Jan. 15–Jan. 22	30–68	Rev-F (20-deg dihedral) baseline
1998	20-in. M6	6763	Feb. 17–Mar. 4	69–203	Rev-F discrete roughness
1998	20-in. M6	6769	April 3–April 17	1–123	Rev-F bowed panels
1998	20-in. M6	6770	May 22–June 24	1–185	Rev-F attach-line roughness
1998	20-in. M6	6777	Aug. 5–Aug. 12	1–40	Rev-F blade vs sting
1999	20-in. M6	6786	May 3–May 14	1–84	Rev-G extended bowed panels

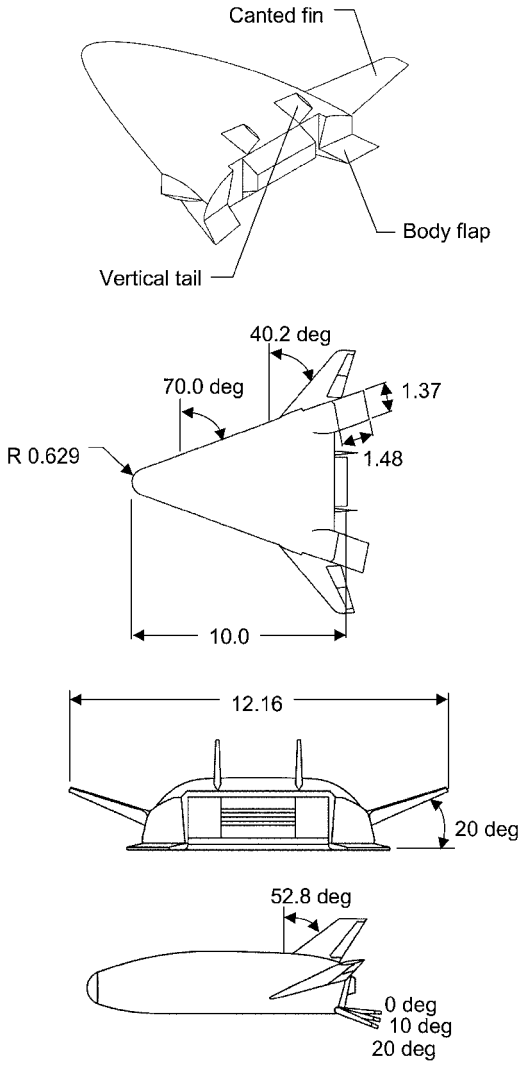

Fig. 1 Dimensions (in inches) for 0.013-scale X-33 model of configuration F Rev-F.

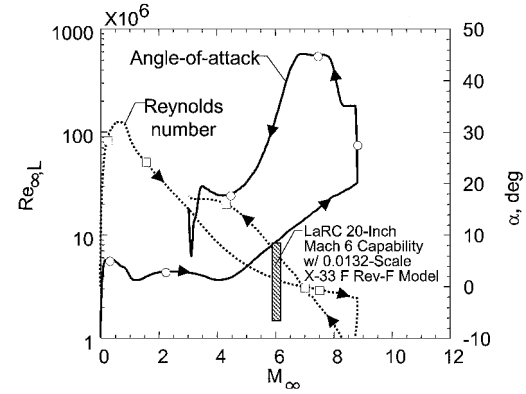

Fig. 2 Typical X-33 trajectory.

for X-33 (Ref. 8). Since the time of these publications, additional heating tests have been completed that supplemented the original database and accommodated design changes to the vehicle outer mold lines. Key Phase II experimental and computational aeroheating results are presented in this reference and in two companion papers by Berry et al.[9] and Hollis et al.[10] An extensive testing effort was made to examine the effects of both discrete roughness and distributed roughness [in the form of a simulated array of thermally bowed metallic thermal protection system (TPS) panels] on transition. The sensitivity of X-33 boundary-layer transition to this wavy wall and the validity of the discrete roughness defined Re_θ/M_e transition criteria off vehicle centerline have been investigated.[9] Additional Navier–Stokes computations were performed at NASA LaRC[10] and NASA Ames Research Center (ARC),[11] and detailed comparisons with the more recent wind-tunnel data have been made to validate computational techniques used in predicting complex three-dimensional flowfields.[9] The experimental results were obtained in the NASA LaRC Aerothermodynamic Facilities Complex (AFC).[12] Over 1100 tunnel runs from 16 different entries in two facilities have been completed since August 1996. Table 1 provides a list of all of the wind-tunnel tests that have been completed to date in support of X-33 aeroheating since the Phase II down select.

The purpose of this paper is to update and present an overview of the most current experimental measurements to characterize the X-33 windward and leeward aeroheating environments, and the paper will focus on the heating associated with a nominally smooth surface. The wind-tunnel data in this report were obtained from the NASA LaRC 20-Inch Mach 6 Air Tunnel. In terms of Mach and Reynolds number simulation, an early X-33 flight trajectory (9d-3) considered by Lockheed Martin (Fig. 2) indicates that the 63-ft-long flight vehicle would experience a length Reynolds number Re_L between 4×10^6 and 8×10^6 at a freestream Mach number of 6. This range of length Reynolds number can be produced in the NASA LaRC 20-Inch Mach 6 Air Tunnel with an appropriately sized model. A Re_L range from 0.4×10^6 to 6.7×10^6 is achieved in this tunnel with a 10-in. model length. The current flight trajectory from Edwards Air Force Base into Michael Air Force Base has been modified from the preliminary trajectory (9d-3) shown and would place peak stagnation point heating to a reference hemisphere during ascent near Mach 9 at $\alpha = 13$ deg and during descent near Mach 7 at $\alpha = 32$ deg.

Test techniques that were utilized during these tests include thermographic phosphors, which provide global surface heating images; oil flow, which provides surface streamline information; and schlieren, which provides shock system details. Parametrics included in these tests at Mach 6 were a large range of angles of

attack to cover ascent and descent conditions ($-5 < \alpha < 40$ deg), unit Reynolds number (Re/ft between 1×10^6 and 8×10^6), and body-flap deflections (δ_{BF}, $= 0$, 10, and 20 deg). Emphasis will be placed on the body-flap surface heating augmentation due to deflection. Sample comparisons with CFD predictions (details provided in Ref. 10) are included and are used to assess the state of the windward surface boundary layer. Extrapolation and comparison of laminar wind-tunnel heating measurements to flight surface temperature predictions are made.

X-33 Body Shape Evolution and Description

The design of the Lockheed Martin X-33 lifting body that emerged from the phase 1 competition drew on a synthesis of work performed by the U.S. government and industry over the last few decades.[13,14] The X-33 body resembled a blunted slab with a delta-shaped planform. Two body flaps trailed from the lower surface outboard of the base mounted linear aerospike engine. These flaps, along with a pair of canted fins and a single vertical tail, would be employed for aerodynamic control. Aerodynamic wind-tunnel tests conducted in government laboratories [NASA LaRC[15,16] and NASA Marshall Space Flight Center (MSFC)[14]] and commercial facilities continued after Phase I down select with the goal of optimizing aerodynamic performance across the speed range. Although the basic lifting body shape has been maintained throughout the development, changes to the vehicle have occurred as the aerodatabase matured. In the past, aeroheating information has significantly lagged behind aerodynamics due to model and instrumentation complexities associated with aerothermodynamic testing. The timeframe of the X-33 program coupled with the recent development of the two-color global phosphor thermography technique[17–19] presented NASA LaRC with the first opportunity to conduct an aerothermodynamic screening/trade in parallel with aerodynamic development.

Phase II aerodynamic optimization studies produced a series of X-33 configurations with outer mold line (OML) changes of sufficient significance to warrant several aeroheating assessment/trade studies. The slab-delta configuration that emerged from the Phase I down select and was used in the early part of Phase II heating tests was designated by Lockheed as 603B1001D. This initial OML was more commonly referred to in the aeroheating design community as the D-loft. The subsequent configuration OML, the F loft Rev-C (604B0002C), differed from the D-loft in that it had twin vertical tails and incorporated some modifications that changed the nose shape slightly and changed the base region (in the vicinity of the engine). The nosecap changes were made to simplify the construction of the metallic TPS panels. Aerodynamic improvements to this vehicle shape resulted in F-loft Rev-F (604B0002F), as shown in Fig. 1. It has the same forebody shape as F-loft Rev-C, but the dihedral of the 0012-64 airfoil canted fins was lowered from 37 to 20 deg (to improve pitch-trim characteristics across the speed range), and the negative fin incidence increased by 2 deg. Finally, the size of the body flaps and vertical tails was increased (to improve trim characteristics and low-speed lateral–directional stability, respectively). The last OML iteration that has undergone heating tests at LaRC is known as F-loft Rev-G (604B0002G). Small protrusions on the leeward surface near the vertical tails were added to accommodate internal structural changes, and the canted fin body fillet was modified. Although other more recent systematic configuration changes have resulted in minor vehicle OML modifications, these changes were not significant enough to warrant construction of new models and additional wind-tunnel testing.

Experimental Methods

Models

A majority of the cast ceramic aeroheating models are a 10-in.-long 0.0132-scale representation of the proposed 63-ft-long (from nose to the end of the aerospike engine base) X-33 F-loft Rev-F (604B0002F) flight vehicle. In addition to configuration assessment of the X-33 OML revisions ($L = 10$ in.), an attempt to characterize qualitatively the influence of model size on tunnel partial blockage effects was made. This was accomplished by limited testing of two smaller scale Rev F models ($L = 5.7$ and 6.5 in.).

Over 70 ceramic models were fabricated in support of the NASA LaRC X-33 aerothermodynamic program, all of which share a common construction technique. A rapid prototyping technique was first used to build a resin stereolithography (SLA) model with various detachable body flaps on both the port and starboard region of the base of the vehicle. The SLA resin model was then assembled with the desired control surface settings and served as a pattern to construct molds from which the cast ceramic model configurations were made. A magnesia ceramic was used to backfill the ceramic shells, thus providing strength and support to the sting support structure.

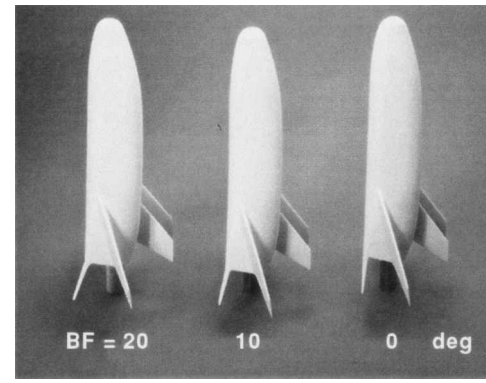

Fig. 3 X-33 F Rev-F ceramic models with three flap deflections.

A photograph of three 0.0132-scale (10-in.) Rev-F model configurations with the various body-flap deflections are shown in Fig. 3. Typically, two casts of each configuration were made, the primary being immediately prepared for testing and the backup shell held in reserve, in case of problems with the primary. To obtain accurate heat transfer data with the phosphor technique, the models are cast with a material with low thermal diffusivity and well-defined, uniform, isotropic thermal properties. The phosphor coatings typically do not require refurbishment between wind-tunnel runs and have been measured to be approximately 0.001 in. thick. Details concerning the model fabrication technique and phosphor coating can be found in Refs. 20 and 21. Fiducial marks were placed on the model surface to assist in determining spatial locations accurately. Once the phosphor testing was completed, the untested backup models were prepared (spray coated and kiln fired with a thin black glazing) for use as oil flow and schlieren models.

Facility Description

The X-33 aeroheating test series was conducted in two hypersonic blowdown facilities that are part of the NASA LaRC AFC. Detailed descriptions of and calibration results from the facilities within the complex can be found in Ref. 12. A brief description of the NASA LaRC 20-Inch Mach 6 Air Tunnel follows because a majority of the tests were in this facility.

The NASA LaRC 20-Inch Mach 6 Air Tunnel uses heated, dried, and filtered air as the test gas. Typical operating conditions for the tunnel are stagnation pressures ranging from 30 to 500 psia, stagnation temperatures from 760 to 1000°R, and freestream unit Reynolds numbers from 0.5×10^6 to 8×10^6/ft. A two-dimensional, contoured nozzle is used to provide nominal freestream Mach numbers from 5.8 to 6.1. The test section is 20.5×20 in. The nozzle throat is 0.399×20.5 in. A bottom-mounted model injection system can insert models from a sheltered position to the tunnel centerline in less than 0.5 s. Run times up to 15 min are possible with this facility, although for the current heat transfer and flow visualization tests, the model residence time in the flow is limited to only a few seconds. Flow conditions were determined from the measured reservoir pressure and temperature and the measured pitot pressure at the test section.

Test Conditions and Setup

Nominal reservoir and corresponding freestream flow conditions for the NASA LaRC 20-Inch Mach 6 Air Tunnel is presented in Ref. 21. The freestream properties were determined from the measured reservoir pressure and temperature and the measured pitot pressure at the test section. The reservoir pressure $p_{t,1}$ was measured

with two silicon sensors having a full-scale rating of 150 or 500 psia, depending on the operating condition of the tunnel. The reservoir temperature $T_{t,1}$ was measured with two iron–constantan thermocouples inserted through the wall of the settling chamber. Test-section wall static and pitot pressures were monitored and compared to tunnel empty conditions to assess if model blockage effects existed. No significant differences in pitot pressure were measured, and it was concluded that significant blockage did not exist (up to 40-deg angle of attack, the limit of the tests). The ratio of projected model frontal area to tunnel cross-sectional area for the present test was 0.1 (at $L = 10$ in. and $\alpha = 40$ deg).

All models were supported by a base-mounted cylindrical sting with the exception of two models ($L = 6.5$ and 5.7 in.) that were blade supported from the leeside to assess support interference effects. Details of the X-33 ceramic heat transfer model installation in the NASA LaRC 20-Inch Mach 6 Air Tunnel can be found in Ref. 21. The various model configurations were pitched through angle of attack in increments of 5 deg. A limited number of runs were made at incidence angles outside these increments to match conditions at points in the X-33 trajectory of interest to the aerodynamic community. Sideslip was held fixed at 0 deg with the exception of the tests conducted in the NASA LaRC 20-Inch Mach 6 CF_4 Tunnel with a sideslip angle of 4 deg.

Test Techniques

The rapid advances in image processing technology that have occurred in recent years have made digital optical measurement techniques practical in the wind tunnel. One such optical acquisition method is two-color relative-intensity phosphor thermography,[17–19] which is currently being applied to aeroheating tests in the hypersonic wind tunnels of NASA LaRC.[22–24] With this technique, ceramic wind-tunnel models are fabricated and coated with phosphors that fluoresce in two regions of the visible spectrum when illuminated with ultraviolet light. The fluorescence intensity is dependent on the amount of incident ultraviolet light and the local surface temperature of the phosphors. By acquiring fluorescence intensity images of an illuminated phosphor model exposed to flow in a wind tunnel with a color video camera, surface temperature mappings can be calculated on the portions of the model that are in the field of view of the camera. A temperature calibration of the system conducted before the study provides the look-up tables that are used to convert the ratio of the green and red intensity images to global temperature mappings. With temperature images acquired at different times in a wind-tunnel run, global heat transfer images are computed assuming one-dimensional semi-infinite heat conduction. The primary advantage of the phosphor technique is the global resolution of the quantitative heat transfer data. Such data can be used to identify the heating footprint of complex, three-dimensional flow phenomena (e.g., transition fronts, turbulent wedges, boundary-layer vortices, etc.) that are extremely difficult to resolve by discrete measurement techniques. Because models are fabricated and instrumented more rapidly and economically, global phosphor thermography has largely replaced discrete heating instrumentation in NASA LaRC's AFC.

Flow visualization techniques, in the form of schlieren and oil flow, were used to complement the surface heating tests. The NASA LaRC 20-Inch Mach 6 Air Tunnel is equipped with a pulsed white-light, Z-pattern, single-pass schlieren system with a field of view encompassing the entire 20-in. test core. Images were recorded on a high-resolution digital camera, enhanced with commercial software and electronically placed into this report. Surface streamline patterns were obtained using the oil flow technique. Backup ceramic models were spray painted black to enhance contrast with the white pigmented oils used to trace streamline movement. A thin basecoat of clear silicon oil was first applied to the surface, and then a mist of pinhead-sized pigmented-oil drops was applied onto the surface. After the model surface was prepared, the model was injected into the airstream and the development of the surface streamlines was recorded with a conventional video camera. The model was retracted immediately following flow establishment and formation of streamline patterns, and postrun digital photographs were taken.

Data Reduction and Uncertainty

A 16-bit analog-to-digital facility acquisition system acquired flow condition data on all channels at a rate of 20 samples/s. Measured values of $P_{t,1}$ and $T_{t,1}$ are believed to be accurate to within $\pm 2\%$. Heating coefficients were calculated from the global surface temperature measurements using one-dimensional semi-infinite solid heat-conduction equations, as discussed in detail in Ref. 19. Acquisition of the surface temperature data was made at the earliest possible time so as to preserve the semi-infinite solid assumption even for areas such as the body flap and fin. In regions of large temperature gradients or small radius of curvature (such as the nosecap and fin leading edges), the error in the inferred heating coefficient due to transverse conduction effects was minimized by acquisition of the data at these early times. The relative intensity phosphor technique does not necessitate corrections for roll-off angle near the planform edges (such as variable emissivity with an infrared thermography technique). As discussed in Ref. 19, the accuracy of the phosphor system measurement is, to a large degree, dependent on the temperature rise on the surface of the model. For the windward side heating measurements, the phosphor system measurement accuracy is believed to be better than $\pm 8\%$, and the overall experimental uncertainty of the heating data due to all factors is estimated to be $\pm 15\%$ (including uncertainties in the thermal physical properties of the ceramic material). In areas on the model where the surface temperature rise is only a few degrees, that is, leeside or aerospike engine, the estimated overall uncertainty increases to at least $\pm 25\%$. Repeatability for the normalized windward centerline (laminar) heat transfer measurements was found to be generally better than $\pm 4\%$.

Prediction Method

X-33 Rev-F flowfield computations for selected angles of attack and test conditions were performed using the GASP code[25] developed by Aerosoft, Inc. GASP is a three-dimensional, finite volume code that incorporates numerous options for flux-splitting methods, thermochemical and turbulence models, and time-integration schemes. Predicted heating from GASP has been validated against flight data obtained from the shuttle orbiter.[26] In the present work, a perfect gas air model was employed with a Jacobi time integration scheme. Full viscous terms were retained for all three directions. A third-order Roe flux-splitting scheme was used in the normal direction to capture accurately shock and boundary-layer gradients, and third-order van Leer flux-splitting was used in the streamwise and circumferential directions to promote stability. All cases were treated as either fully laminar or turbulent. (The turbulent computations were performed using a modified algebraic Baldwin–Lomax model as discussed in Ref. 10.) Grid description, sensitivity studies, turbulence model, and further details regarding the computational solutions presented in this report may be found in Ref. 10.

Results and Discussion

Preface

The X-33 aeroheating results presented in this paper are organized around specific locations on the vehicle such as body flap, canted fin, etc. Presented in Fig. 4 is the X-33 windward surface detailing the various nomenclature and flow features that will be referred to in the discussions. Flow visualization in the form of schlieren and surface oil flows are used to assist in the analysis of the experimentally measured surface heating. The discussion of results will highlight some of the more relevant conclusions to date; a more complete presentation of flow visualization observations can be found in Ref. 21.

Heating distributions are presented in terms of the ratio of enthalpy-based heat-transfer coefficients h/h_{FR}, where h_{FR} corresponds to the Fay and Riddell[27] stagnation-point heating, to a sphere with radius equal to the wind-tunnel model nose ($R_n = 0.629$ in. for the 0.0132-scale 10-in.-long model). A color bar having a maximum value of $h/h_{FR} = 1$ was selected for visual presentation of the data (except where noted) to maintain consistency when viewing or comparing the images. Therefore, in areas where the measured local heating exceeded the stagnation point reference value ($h/h_{FR} > 1$), such as the deflected body flaps or fin leading edges, a gray color has

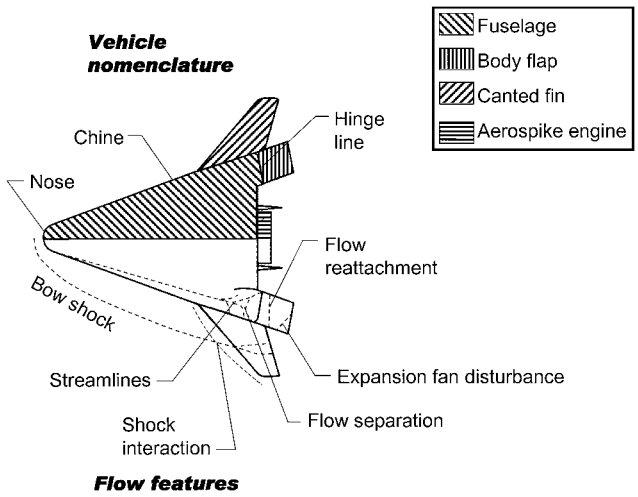

Fig. 4 X-33 Vehicle nomenclature and flow features.

been assigned to the data. On the contour scale, the colors tending toward red indicate areas of higher heating (temperatures), whereas the colors toward blue represent areas of lower heating.

Windward Fuselage

The global effect of Reynolds number on the windward surface heating at Mach 6, $\alpha = 40$ and 20 deg, and $\delta_{BF} = 20$ deg is shown in Figs. 5a–5d and 6a–6d, respectively. These two incident angles were selected to illustrate the distinctly different global heating patterns found on the windward surface near the model base. To understand the nature of this elevated heating, windward centerline heating distributions at $\alpha = 40$ deg over a range of Reynolds numbers are compared with laminar and turbulent prediction in Fig. 7. Comparisons to laminar and turbulent predictions at other angles of attack can be found in Refs. 9 and 10. At the highest Reynolds numbers tested, the experimental heating distributions reveal a departure from the laminar prediction near $X/L = 0.4$. This departure suggests that the boundary layer is transitioning to a turbulent state. (For these test results, the model surface was considered smooth and transition was not forced via applied discrete roughness.) Thus, it is reasonable to hypothesize that the progression of heating images in Figs. 5 and 6 display the evolution of the laminar windward boundary layer at $Re_\infty/\text{ft} = 1 \times 10^6$ to the transitional/turbulent state observed at $Re_\infty/\text{ft} = 8 \times 10^6$. As expected, boundary-layer transition first appeared at the aft end of the model and was found to move forward with increasing Reynolds number. The transition onset Reynolds numbers should not be applied directly to flight due primarily to the adverse effect of tunnel noise and inherent surface roughness of the phosphor-coated ceramic models (which may be different from that found on the metallic surface of the flight vehicle[28,29]).

Consistent with earlier observations[8] made on an X-33 D-loft (603B1001D) forebody, distinctive patterns of the transition region are observed with angle of attack. Figures 8a–8c illustrate the significant differences found at $\alpha = 20$, 30, and 40 deg angles of attack at a constant unit Reynolds number of 8×10^6. At $\alpha = 20$ deg (Fig. 8a), two transition regions symmetric about the centerline are observed. As incidence angle is increased, the regions merge (Fig. 8b) and eventually coalesce into a single parabolic shape at $\alpha = 40$ deg (Fig. 8c). Experimental surface streamline patterns at a unit Reynolds number of 4×10^6 (Figs. 9a–9c) indicate boundary-layer inflow toward the model centerline at $\alpha = 20$ deg. The inflow of surface streamlines (Fig. 9a) results in a flow convergence on the windward centerline, which would thicken the boundary layer locally. The degree of forebody boundary-layer inflow at lower incidence angles was not observed to vary with Reynolds number. The inflow suggests that crossflow may be the mechanism responsible for transition at the higher Reynolds number (Fig. 8a). When the sensitivity of the color scale was increased (not shown), the presence of heating striation patterns at low incidence angles was revealed. It is believed that an array of streamwise-orientated boundary-layer vortices exist on the windward surface and reveal themselves

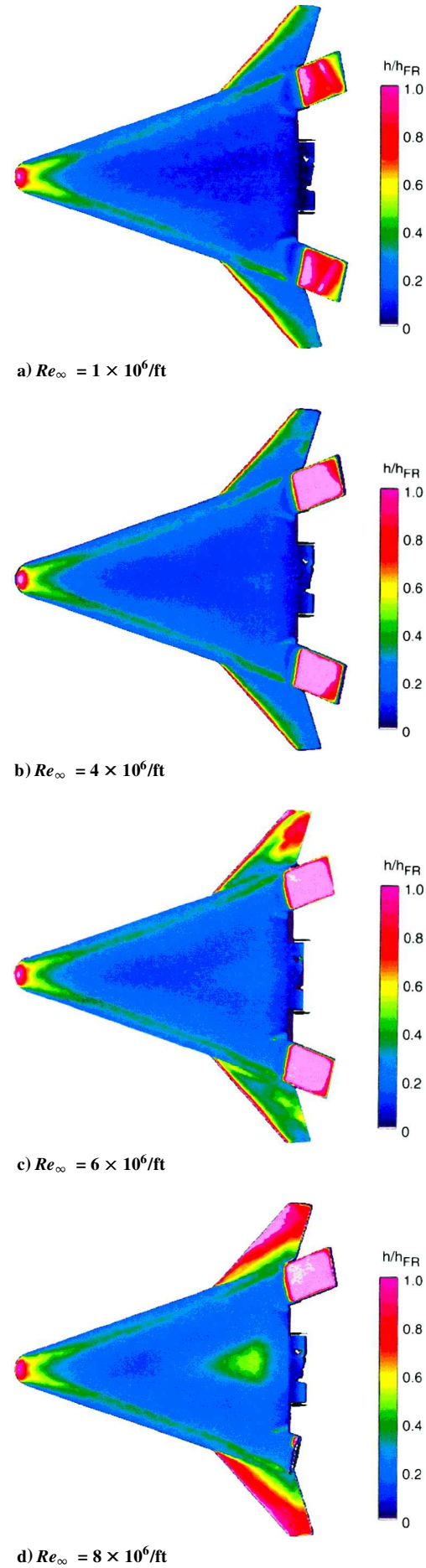

a) $Re_\infty = 1 \times 10^6$/ft

b) $Re_\infty = 4 \times 10^6$/ft

c) $Re_\infty = 6 \times 10^6$/ft

d) $Re_\infty = 8 \times 10^6$/ft

Fig. 5 Effect of Reynolds number on windward heating patterns; $M = 6$, $\alpha = 40$ deg, and $\delta_{BF} = 20$ deg.

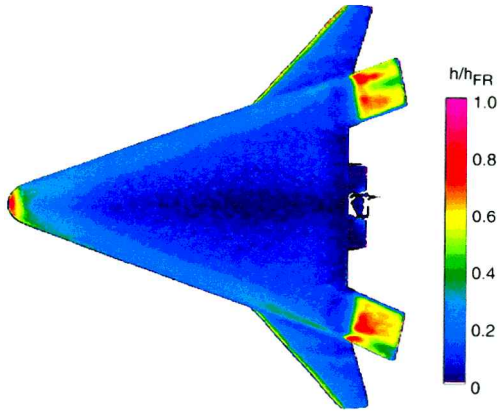

a) $Re_\infty = 1 \times 10^6$/ft

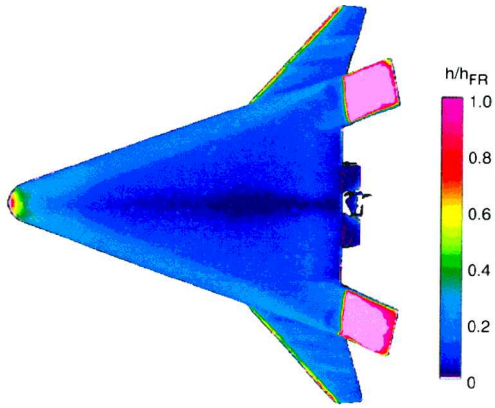

b) $Re_\infty = 4 \times 10^6$/ft

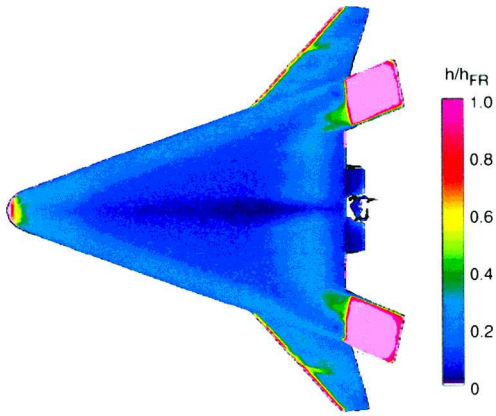

c) $Re_\infty = 6 \times 10^6$/ft

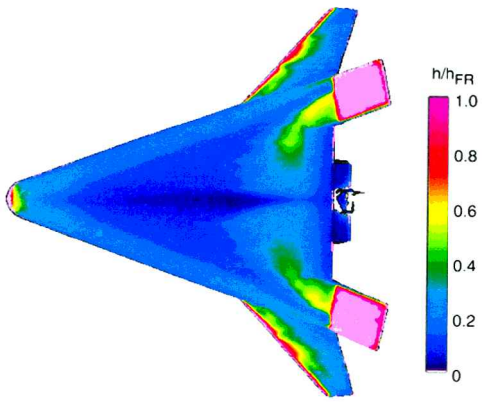

d) $Re_\infty = 8 \times 10^6$/ft

Fig. 6 Effect of Reynolds number on windward heating patterns; $M = 6$, $\alpha = 20$ deg, and $\delta_{BF} = 20$ deg.

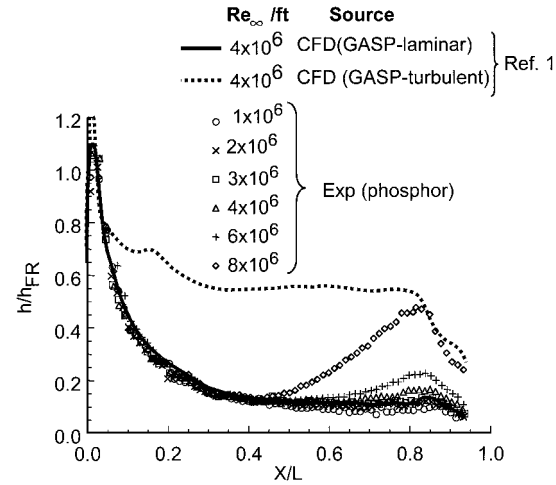

Fig. 7 Windward centerline heating comparisons with laminar and turbulent predictions; $M_\infty = 6$ and $\alpha = 40$ deg.

through local increases in surface shear and, thus, heating. This vortex formation is believed to be indicative of the onset of three-dimensional, crossflow-induced transition from laminar to turbulent flow. The appearance of heating striatia from vortices entrained within supersonic/hypersonic boundary layers has been inferred from flight measurements as well as observations in hypersonic wind tunnels; see Ref. 30 for a more complete review of this phenomenon.

Asymmetric boundary-layer transition on the windward surface chine in the vicinity of the fin/body junction was observed on a few isolated occasions during the test series (see Fig. 8b). This transition was attributed to (unintentional) isolated surface roughness in the phosphor coating created from the impacts of small particulates (of less than 5 μm) on the ceramic model. Although this observation initially suggested heightened sensitivity of the chine to transition, a correlation of isolated roughness data revealed that the off-centerline locations were no more sensitive than those on centerline.[9]

Windward Body Flap

Body-flap deflections of 0, 10, and 20 deg were tested to cover the anticipated deflection range. The flow features and resulting surface heating on the deflected flaps was complex and was in large part determined by the extent of boundary-layer separation ahead of the flap and subsequent flow reattachment. In turn, the control surface flow separation was largely determined by the state of the boundary layer approaching the flaps. As inferred from the $\alpha = 40$ deg surface heating patterns in Figs. 5a–5c, the flow leading up to the deflected control surface is laminar (because transition is limited to the center region only) and appears to separate ahead of the flap hinge line (the cooler region upstream of the hingeline). The off-centerline transition found at the higher Reynolds numbers for $\alpha = 20$ deg (Figs. 6b–6d) reduces or nearly eliminates this separated region.

At low Reynolds numbers, however, the laminar separation region at the flap hinge line persists. The surface streamlines associated with laminar separation at $Re_\infty/\text{ft} = 2 \times 10^6$ from $\delta_{BF} = 20$ deg is shown in Figs. 10a–10c for $\alpha = 20$, 30, and 40 deg. This flow separation region becomes smaller with increasing angle of attack. The circulation of separated flow upstream of reattachment was highly three dimensional with a strong curvature of the streamlines away from the body-flap centerline. This outboard directed flow spillage did not appear to influence the flow over the nearby canted fin (as was observed on several X-33 Phase I configurations). The flow reattachment downstream on the body flap was observed to be in close proximity and nearly parallel to the hinge line at all angles of attack, suggesting locally higher heating in this area. The body-flap hinge line gap is planned to be sealed to prevent the circulation of this high-energy flow into a cavity. Expansion of the flow around the body-flap edges is indicated by the local streamline curvature; the outboard curvature is most pronounced at $\alpha = 40$ deg and is indicative of a stronger lateral pressure gradient at the higher angles of attack.

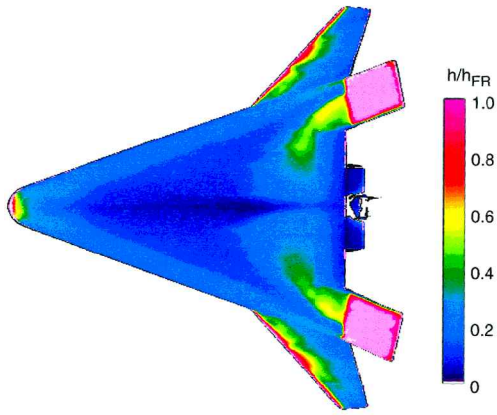

a) α = 20 deg

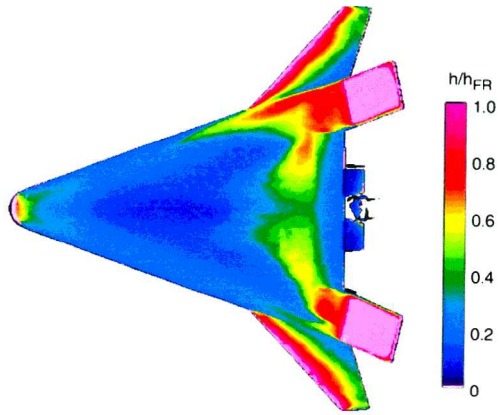

b) α = 30 deg

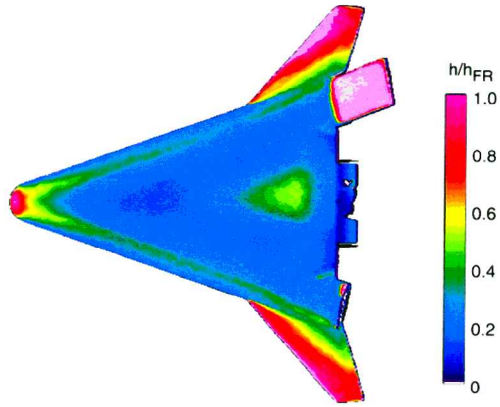

c) α = 40 deg

Fig. 8 Effect of angle of attack on windward transition patterns; M_∞ = 6, δ_{BF} = 20 deg, and Re_∞ = 8 × 10^6/ft.

A 20-deg deflected body flap at angles of attack of 30 and 40 deg produced a disturbance in the flap streamline pattern (Figs. 10b and 10c). Computational predictions of the corresponding flowfield (Ref. 15) indicated the interaction of the deflected flap shock with the bow shock. The outboard location of the X-33 body flaps (in contrast, for example, to the shuttle orbiter body flap) locates the body-flap shock system in close proximity to the bow shock. Computed flowfield results show that the resulting interaction produced an expansion fan that impinged on the body flap in the same spatial orientation as seen in the experimental heating (Fig. 5a) and surface streamline patterns (Figs. 10b and 10c). A typical side view schlieren image, Fig. 11, at $\alpha = 30$ deg, $\delta_{BF} = 20$ deg, and $Re_\infty/\text{ft} = 2 \times 10^6$ is presented to characterize the shock system in this region. The sensitivity of the schlieren system did not permit the detection of the expansion wave disturbance. This type of surface disturbance on

a) α = 20 deg

b) α = 30 deg

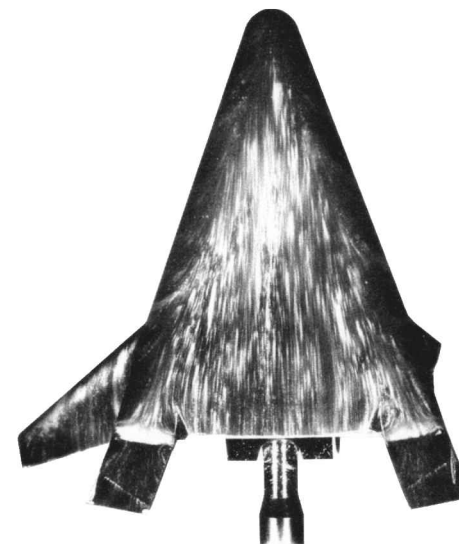

c) α = 40 deg

Fig. 9 Effect of angle of attack on windward surface streamlines; M_∞ = 6, δ_{BF} = 20 deg, and Re_∞ = 4 × 10^6/ft.

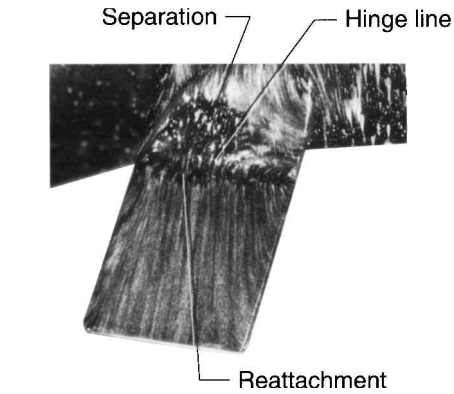

a) α = 20 deg

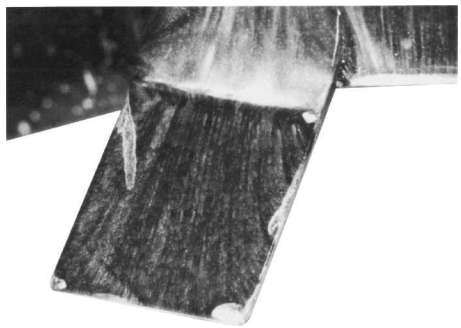

b) α = 30 deg

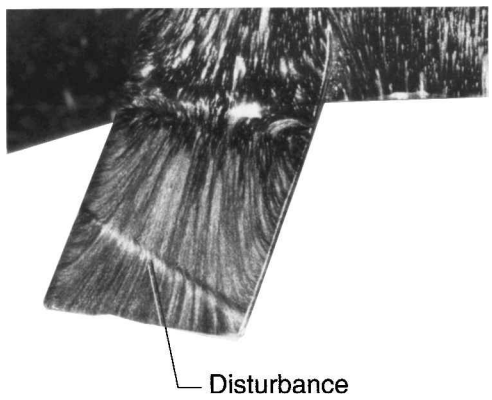

c) α = 40 deg

Fig. 10 Effect of angle of attack on body-flap surface streamlines; M_∞ = 6, δ_{BF} = 20 deg, and Re_∞ = 2 × 10^6/ft.

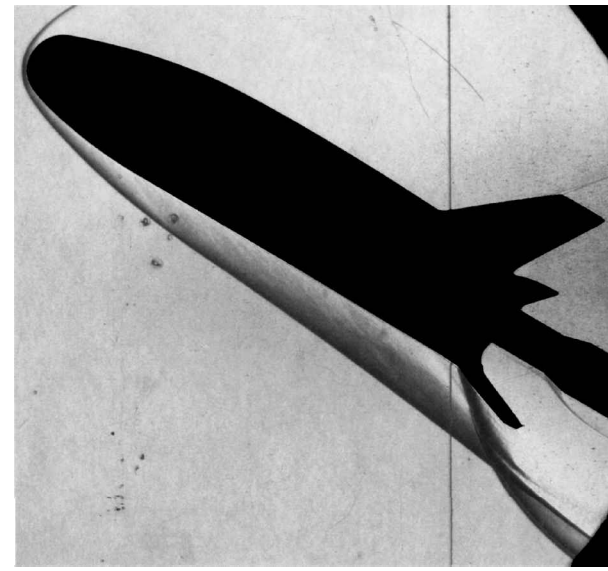

Fig. 11 Schlieren image; M_∞ = 6, α = 30 deg, δ_{BF} = 20 deg, and Re_∞ = 2 × 10^6/ft.

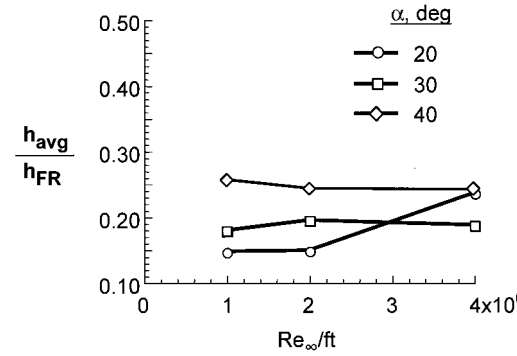

Fig. 12 Effect of angle of attack and Reynolds number on averaged undeflected body-flap heating; M_∞ = 6 and δ_{BF} = 0 deg.

the flap had not been observed on earlier X-33 configurations due to shorter length body flaps. Localized increases in body-flap surface heating corresponding to flow reattachment near the hingeline and from the expansion fan disturbance were observed (Fig. 5a) and will be discussed in more detail later. The local heating peak from the disturbance was observed at all Reynolds numbers, but because the color bar scale for this report was set to provide the best sensitivity for presentation of windward surface transition images (on the fuselage), the body-flap data are visually all off-scale.

To provide heating trends on the flaps in the absence of flow separation, the entire undeflected body-flap ($\delta_{BF} = 0$ deg) surface heating was averaged and presented (Fig. 12) as a function of Reynolds number. As expected, the undeflected flap surface heating increased with angle of attack. The averaged heating to the undeflected flap was essentially invariant with Reynolds number for $\alpha = 30$ and 40 deg, suggesting that the attached flow over the control surface remained laminar at these incident angles. The increase in the averaged undeflected flap heating measured at $Re_\infty/\text{ft} = 4 \times 10^6$ for $\alpha = 20$ deg has been attributed to the off-centerline transitional/turbulent boundary layer on the forebody (upstream of the flap; see progression of images in Figs. 6a–6d) spreading onto the undeflected control surface.

The effect of control surface deflections on averaged flap surface heating at $Re_\infty/\text{ft} = 4 \times 10^6$ for $\alpha = 30$ and 40 deg is shown in Figs. 13a and 13b. Figures 13 present data obtained with a laminar (Fig. 13a) and turbulent (Fig. 13b) boundary layer approaching the flap (details of the boundary-layer tripping method can be found in Refs. 10 and 22). The data presented in Figs. 13a and 13b are presented in the form of a ratio of deflected to undeflected flap heating. (In Figs. 13a and 13b, the undeflected flap reference heating was obtained for both laminar and turbulent conditions.) Presented in this fashion, these experimentally derived heating augmentation factors may be used with $\delta_{BF} = 0$ deg flight analytic solutions to provide a preliminary estimate of deflected flap heating levels in flight. Heating augmentation for angles of attack of 30 and 40 deg was found to increase linearly with flap deflections of 20 and 30 deg. Maximum heating augmentation values of 5–7.5 over the laminar undeflected reference case and 2–3 over the turbulent undeflected reference were measured. The heating augmentation factors were insensitive to the state of the approaching boundary layer (laminar or turbulent), which suggests that the boundary layer downstream of reattachment on the flap was transitional if not fully turbulent.

Although the averaged body-flap heating was useful to examine trends, the local flow on the deflected flaps was observed to be quite complex. With the exception of the lowest Reynolds numbers, the heating levels found on the deflected body flaps generally meet or exceed the theoretical reference stagnation level h_{FR}. Right and

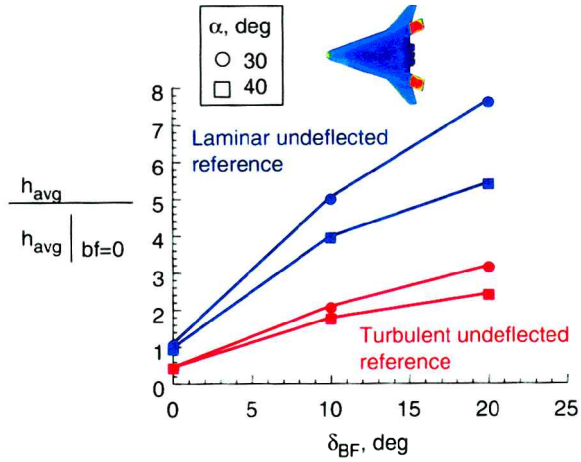

a) Boundary layer approaching flap: laminar

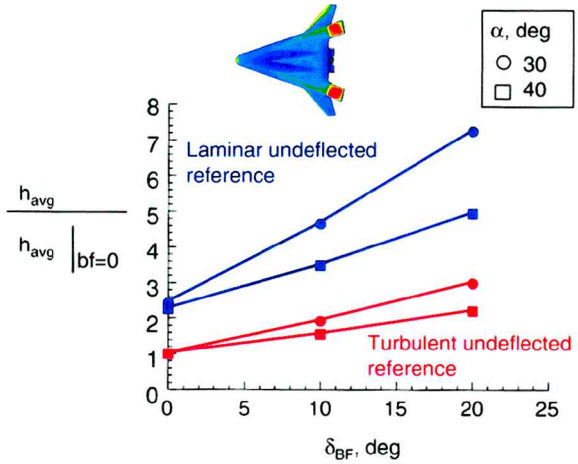

b) Boundary layer approaching flap: turbulent (tripped)

Fig. 13 Averaged deflected body-flap heating normalized to laminar and turbulent undeflected reference $M_\infty = 6$ and $Re_\infty = 4 \times 10^6$/ft.

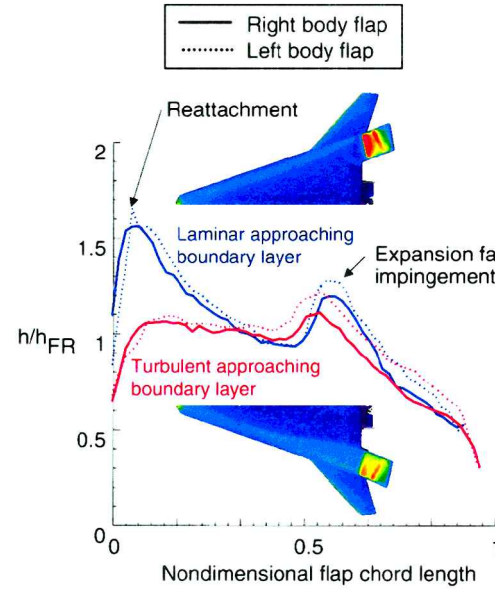

Fig. 14 Body-flap centerline heating distribution; $M_\infty = 6$, $\alpha = 40$ deg, $\delta_{BF} = 20$ deg, and $Re_\infty = 2 \times 10^6$/ft.

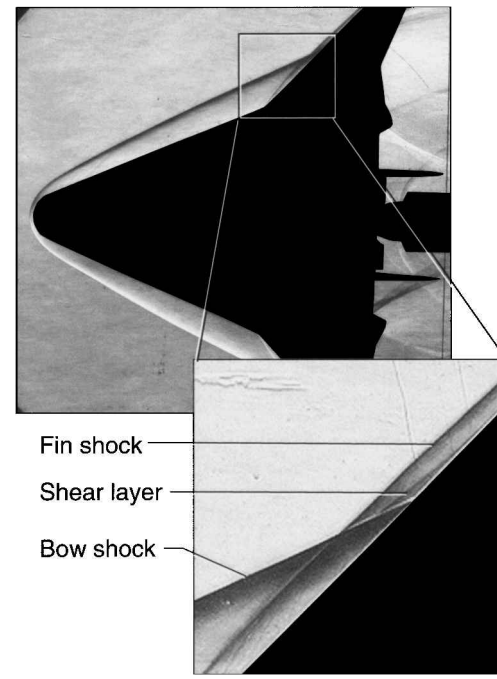

Fig. 15 Schlieren image of bow/fin-shock interaction; $M_\infty = 6$, $\alpha = 30$ deg, $\delta_{BF} = 20$ deg, and $Re_\infty = 4 \times 10^6$/ft.

left body-flap centerline heating distributions extracted from images taken at $\alpha = 40$ deg, $\delta_{BF} = 20$ deg, and $Re_\infty/\text{ft} = 2 \times 10^6$ are shown (Fig. 14) for both a laminar and turbulent (tripped) boundary layer approaching the flap. For a laminar boundary layer approaching the deflected flap, the local centerline heating peaks from flow reattachment ($h/h_{FR} = 1.6$) and expansion fan impingement ($h/h_{FR} = 1.3$) are measured at approximately 5 and 55% flap chord length and are spatially consistent with surface oil-flow observations. The local heating peak from flow reattachment was reduced nearly 60% when the boundary layer was forced turbulent upstream of the deflected flap. Based on this observation, it is believed that the turbulent boundary layer approaching the flap reduced or eliminated flow separation and produced turbulent heating levels. The laminar separation yields flow reattachment that is transitional and heating that is characteristically higher than turbulent results. Computations[15] suggest that the secondary heating peak downstream of reattachment is the result of a thinning boundary layer produced from the head of the expansion wave system impinging on the flap. The rapid decrease in heating downstream of the secondary peak correlates with a predicted drop in surface pressure from the expansion fan tail.

Canted Fin

The shock shape about the X-33 F Rev-F model is shown in planform view in Fig. 15 for $\alpha = 30$ deg, $\delta_{BF} = 20$ deg, and $Re_\infty/\text{ft} = 2 \times 10^6$. The bow shock was observed to interact with the canted fin leading edge at all angles of attack tested. Inherently three dimensional, the observed shock orientations (inset, Fig. 15) most closely resemble a two-dimensional Type VI interaction described by Edney,[31] which is known to produce a shear layer and expansion fan. Depending on model angle of attack, this shear layer is thought to be swept over the fin upper and/or lower surface, producing local perturbations in fin surface heating. The surface effect from the shock interaction was not easily discernable from the streamline patterns on the fins (Figs. 9a–9c) but was more readily identified in the surface heating images (Figs. 6a–6d). The fin windward surface heating resulting from this interaction is complex and more distinct at lower angles of attack. On the canted fin windward surface, elevated heating from boundary-layer transition (associated with the bow/fin–shock interaction and possible leading-edge attachment line contamination[32]) occurs for unit Reynolds numbers in excess of $Re_\infty/\text{ft} = 4 \times 10^6$ (Figs. 5c, 5d, 6c, and 6d). Asymmetric boundary-layer transition on the windward fin surface was observed on a few isolated occasions during the test series (see Fig. 5c) and was attributed to (unintentional) isolated surface roughness (discussed earlier) on the fin leading edge.

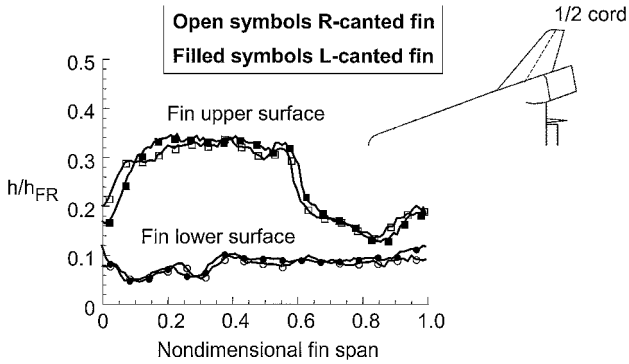

a) $\alpha = 0$ deg

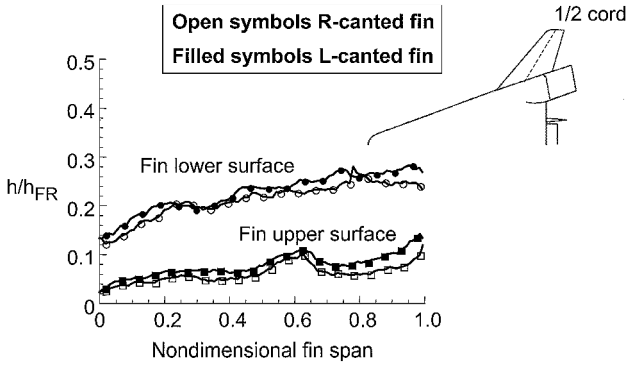

b) $\alpha = 30$ deg

Fig. 16 Canted fin heating distribution; $M_\infty = 6$, $\delta_{BF} = 20$ deg, and $Re_\infty = 4 \times 10^6$/ft.

At high angles of attack characteristic of hypersonic entry, the X-33 canted fin lower surface would be exposed to the flow and, in the traditional sense, called a windward surface. At low angle of attack representative of ascent, however, this same fin surface would be shadowed from the flow (due to negative fin incidence). Because of this situation, the fin surfaces in the following section are referred to as upper and lower. Canted fin upper and lower surface heating distributions extracted from images taken at $\alpha = 0$ and 30 deg, $\delta_{BF} = 20$ deg, and $Re_\infty/\text{ft} = 4 \times 10^6$ are shown in Figs. 16a and 16b. The heating distributions were taken at the fin half-chord station. At a low incidence angle characteristic of ascent, the surface heating to the canted fin lower surface was less than that measured on the upper fin surface (due to the negative fin incidence). At $\alpha = 0$ deg (Fig. 16a), the heating to the fin lower surface is relatively uniform at this fin chord location with $h/h_{FR} = 0.1$ and with no evidence of locally large increases in surface heating from the bow/fin–shock interaction. It is believed that the disturbances (shear layer) from the interaction are swept over the fin upper surface, producing locally elevated heating. For example, heating to the undisturbed outboard 40% of the fin was found to be near $h/h_{FR} = 0.15$, whereas the disturbed inboard 60% of the fin had a heating peak of approximately $h/h_{FR} = 0.35$. As anticipated, an increase in angle of attack to 30 deg (Fig. 16b) produced heating levels on the fin lower surface that are elevated above that measured on the upper surface.

As noted earlier, boundary-layer transition associated with the bow/fin–shock interaction occurs for unit Reynolds numbers in excess of $Re_\infty/\text{ft} = 4 \times 10^6$. Elevated fin heating from shock/shock induced boundary-layer transition is apparent in the extracted fin heating distributions measured over a range of Reynolds numbers and shown in Figs. 17a and 17b. The disturbance from the bow–shock interaction on the fin lower surface at $\alpha = 30$ deg (Fig. 17a) is not readily discernable at the fin half-chord station until $Re_\infty/\text{ft} = 4 \times 10^6$. Similarly, the transitional effects from the shock interaction on the fin upper surface at $\alpha = 0$ deg (Fig. 17b) are not apparent below $Re_\infty/\text{ft} = 4 \times 10^6$.

Engine

Impingement of the separated flow off the windward fuselage base onto the lower surface of the linear aerospike nozzle was inferred

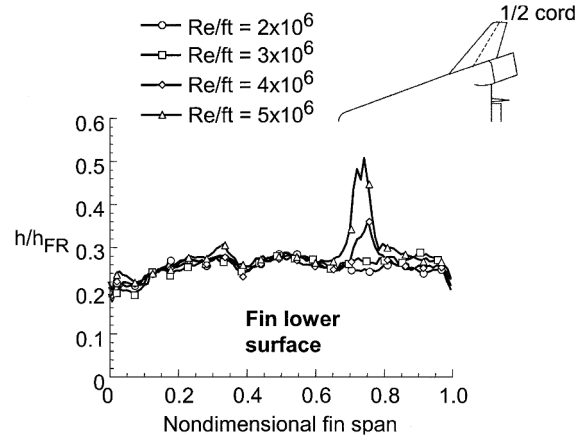

a) $\alpha = 30$ deg

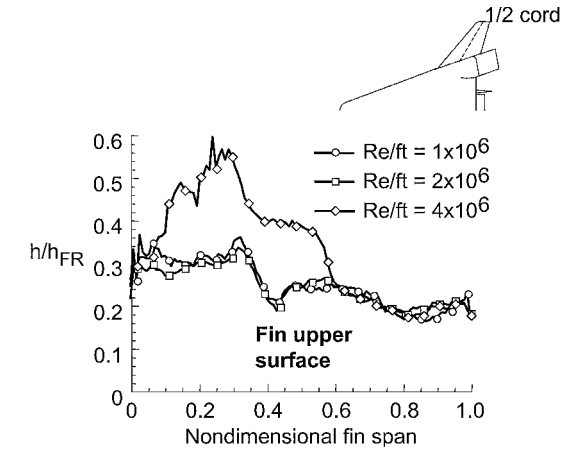

b) $\alpha = 0$ deg

Fig. 17 Effect of Reynolds number on canted fin heating distribution; $M_\infty = 6$ and $\delta_{BF} = 20$ deg.

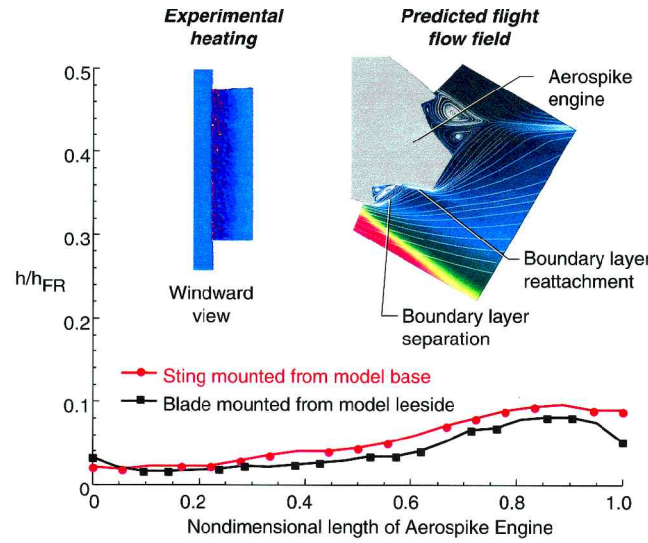

Fig. 18 Heating distribution on aerospike engine; $M_\infty = 6$, $\alpha = 40$ deg, $\delta_{BF} = 20$ deg, and $Re_\infty = 4 \times 10^6$/ft (flight prediction courtesy K. Weilmuenster); $\alpha = 40$ deg.

from elevated heating measured at this location (see Figs. 5b–5d). Extracted heating distributions at $\alpha = 40$ deg and $Re_\infty/\text{ft} = 4 \times 10^6$ (Fig. 18) indicated that, at reattachment, peak heating was on the order of 10% of the nose stagnation value. Surprisingly, support system interference effects (leeside blade mount vs base sting mount) in this region were not apparent. Flowfield computations[11] at flight conditions have also predicted flow impingement on the nozzle, producing heating rates on the order of 5% of the nose stagnation value.

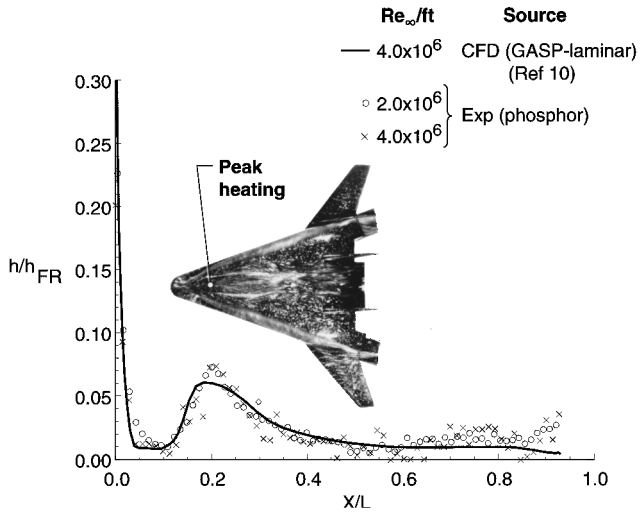

Fig. 19 Upper fuselage centerline heating comparison with laminar prediction; $M_\infty = 6$, $\alpha = 40$ deg, and $\delta_{BF} = 20$ deg.

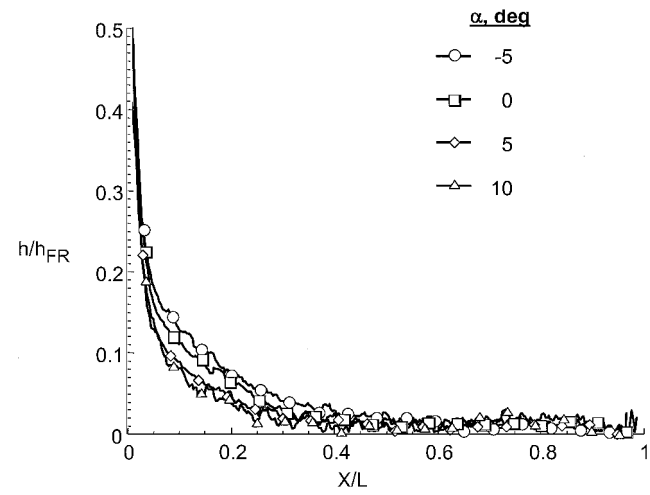

Fig. 20 Effect of angle of attack on upper fuselage centerline heating distributions; $M_\infty = 6$, $\delta_{BF} = 20$ deg, and $Re_\infty = 4 \times 10^6$/ft.

The experimental and theoretical evidence of nozzle flow impingement led to the design of a system to circulate residual hydrogen through the structure during descent to actively cool the nozzle in flight.

Leeward Fuselage

Much lower heating levels generally characterize the thermal environment of a vehicle leeward surface at hypersonic entry angles of attack. Comparison of leeward centerline heating at $Re_\infty/\text{ft} = 2 \times 10^6$ and 4×10^6 with laminar prediction ($Re_\infty/\text{ft} = 4 \times 10^6$) at $\alpha = 40$ deg is shown (Fig. 19). The laminar comparison presented here and at lower angles of attack[10] was generally within the experimental uncertainty (±25%) with the exception near the end of the fuselage. This discrepancy may exist because the model base and wake flow were computationally simplified.[10] The actual flow expansion from the leeside into the wake during the tests might result in the higher heating. No significant Reynolds number effects were observed experimentally, which suggests either that the leeward flow remained laminar or that the difference between laminar and turbulent leeside heating is small. A heating maxima of 7.5% of the stagnation reference value was measured at $X/L = 0.2$.

At angles of attack more representative of ascent, the placement of the X-33 TPS split lines in the vicinity of the nosecap becomes more crucial. At low incidence angles, the upper fuselage is effectively a windward surface. (Recall that vehicle peak heating during ascent occurs near Mach 9, corresponding to $\alpha = 13$ deg.) Laminar centerline heating distributions along the vehicle upper surface at $Re_\infty/\text{ft} = 4 \times 10^6$ for $\alpha = -5$, 0, 5, and 10 deg are shown (Fig. 20). These low-angle-of-attack distributions were obtained as a small part of a validation process aimed at determining TPS split lines.

Extrapolation to Flight

A feature of the phosphor thermography analysis package[18] (IHEAT) is the ability to extrapolate ground-based heating measurements to flight radiation equilibrium wall temperatures. The successful application of this technique to predict flight surface temperatures for both laminar and turbulent conditions was first demonstrated in the X-34 (Refs. 18 and 23) program and later for X-38 (Ref. 24). Based on the initial success with the X-34 data and the good agreement between the X-33 laminar data and GASP prediction presented in this report, phosphor data were extrapolated to flight surface temperatures and compared to an equilibrium laminar GASP flight prediction (Fig. 21). The tunnel data were obtained at $\alpha = 40$ deg, $\delta_{BF} = 20$ deg, and $Re_{\infty,L} = 2 \times 10^6$. Flight conditions at this angle of attack correspond to an altitude of 146,730 ft, velocity of 7045 ft/s, Mach number of 6.6, and a length Reynolds number of 5×10^6. The body flap was omitted for the flight computation. As with the X-34 flight case, no significant real gas effects were anticipated at this X-33 flight condition. The phosphor images were mapped to the three-dimensional vehicle surface geometry via a

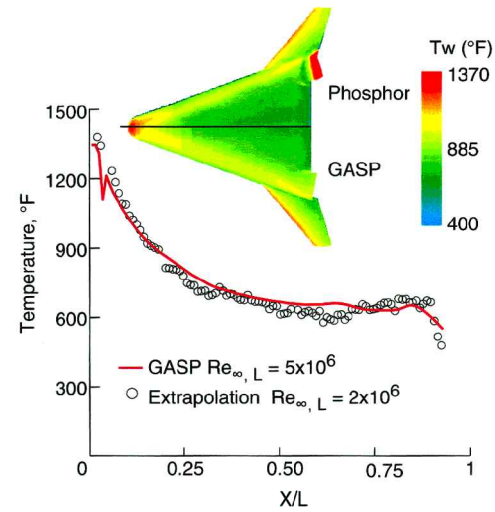

Fig. 21 Extrapolation of laminar experimental centerline data to flight conditions; $M_\infty = 6.6$ and $\alpha = 40$ deg.

new option in the IHEAT code. The global comparison of windward surface temperature presented in Fig. 21 is shown along with data extracted along the centerline. Generally, the surface temperatures compare well over the entire image. The extrapolated wind-tunnel data generally compare to within 50°F of prediction along the centerline. This type of information provided to the designer early in the TPS evaluation process would be invaluable and could potentially result in significant savings of computational time required for flight predictions.

Conclusions

One of the key technologies being demonstrated on the Lockheed Martin X-33 RLV demonstrator is an advanced metallic TPS. The heating environment definition for X-33 incorporates conceptual analysis, ground-based testing, and CFD into the TPS design process. This report provides an overview of the hypersonic aeroheating wind-tunnel program conducted at the NASA LaRC in support of the ground-based testing activities. In the past, aeroheating information has significantly lagged behind aerodynamic information due primarily to model and instrumentation complexities associated with aerothermodynamic testing. The X-33 program was able to take advantage of recent developments in a two-color global phosphor thermography technique, providing the first opportunity to conduct an aerothermodynamic screening/trade study concurrent with aerodynamic tests. The work reported herein served as a baseline for a parallel effort to determine the effect of discrete roughness and distributed roughness due to a bowed panel (TPS) array on boundary-layer transition. The study also provided a laminar and turbulent

heating database with a wide range of parameters from which engineering and benchmark CFD codes were validated against.

Global surface heat transfer images, surface streamline patterns, and shock shapes were measured on 0.013-scale (10-in.) ceramic models of the proposed X-33 configuration in Mach 6 air. The test parametrics included angles of attack from −5 to 40 deg, unit Reynolds numbers from 1×10^6 to 8×10^6/ft, and body flap deflections of 0, 10, and 20 deg. Comparisons of the laminar and turbulent experimental data were performed that also served to assess the state of the windward boundary layer. It was determined that natural transition occurred on the windward surface. The smooth-body transition patterns observed on the windward surface were strongly dependent on angle of attack and were consistent with early Phase II observations. At hypersonic entry incidence angles, a complex surface flow environment was observed on the deflected body flaps downstream of reattachment. Experimental and computational results indicated the presence of shock/shock interactions that produced localized heating on the deflected flaps and boundary-layer transition on the canted fins. At an incidence angle of 40 deg, a laminar boundary layer approaching a 20-deg deflected flap produced a local heating peak ($h/h_{FR} = 1.3$) from a shock/shock interaction. Laminar windward centerline heating data from the wind tunnel was extrapolated to flight surface temperatures and generally compared to within 50°F of flight prediction.

Acknowledgments

Without the assistance of the following individuals this work would not have been possible: Mark Cagle, Joe Powers, Mike Powers, Mark Griffith, Ed Covington, and Tom Burns for model design/fabrication/instrumentation/surface inspection support; John Ellis, Rhonda Manis, Grace Gleason, Melanie Lawhorne, Harry Stotler, Steve Jones, and Jeff Warner for wind-tunnel support; Sheila Wright and Bert Senter for data acquisition assistance; Bill Wood for computational fluid dynamics analysis support; and Richard Wheless for documentation assistance. The authors gratefully acknowledge their contributions and behind-the-scenes work.

References

[1]Bekey, I., Powell, R., and Austin, R., "NASA Studies Access to Space," *Aerospace America*, May 1994, pp. 38–43.

[2]Cook, S. A., "X-33 Reusable Launch Vehicle Structural Technologies," AIAA Paper 96-4523, Nov. 1996.

[3]Freeman, D. C., Jr., Talay, T. A., and Austin, R. E., "Reusable Launch Vehicle Technology Program," International Astronautical Federation, Paper IAF 96-V.4.01, Oct. 1996.

[4]Powell, R. W., Lockwood, M. K., and Cook, S. A., "Road from the NASA Access-to-Space Study to a Reusable Launch Vehicle," International Astronautical Federation, Paper IAF 98-V.4.02, Sept. 1998.

[5]Baumgartner, R. I., and Elvin, J. D., "Lifting Body, an Innovative RLV Concept," AIAA Paper 95-3531, Sept. 1995.

[6]Thompson, R. A., "Review of X-33 Hypersonic Aerodynamic and Aerothermodynamic Development," International Council of the Aeronautical Sciences, Rept. ICA-0323, Aug. 2000.

[7]Hamilton, H., Berry, S., Horvath, T., and Weilmuenster, J., "Computational/Experimental 1998. Aeroheating Predictions for X-33 Phase 2 Vehicle," AIAA Paper 98-0869, Jan. 1998.

[8]Thompson, R. A., Hamilton, H. H., Berry, S. A., and Horvath, T. J., "Hypersonic Boundary-Layer Transition for X-33 Phase 2 Vehicle," AIAA Paper 98-0867, Jan. 1998.

[9]Berry, S. A., Horvath, T. J., Hollis, B. R., Thompson, R. A., and Hamilton, H. H., II, "X-33 Hypersonic Boundary-Layer Transition," *Journal of Spacecraft and Rockets*, Vol. 38, No. 5, 2001, pp. 646–657.

[10]Hollis, B. R., Horvath, T. J., Berry, S. A., Hamilton, H. H., II, and Alter, S. J., "X-33 Computational Aeroheating Predictions and Comparisons with Experimental Data," *Journal of Spacecraft and Rockets*, Vol. 38, No. 5, 2001, pp. 658–669.

[11]Dinesh, P. K., Wright, M. J., Marvin, J. G., Brown, J. L., and Venkatapathy, E., "X-33 Aerothermal Design Environment Predictions: Verification and Validation," AIAA Paper 2000-2686, June 2000.

[12]Miller, C. G., "NASA Langley Research Center Hypersonic Aerodynamic/Aerothermodynamic Testing Capabilities, Present and Future," AIAA Paper 90-1376, June 1990.

[13]Reed, R. D., "Wingless Flight, the Lifting Body Story," NASA SP-4220, Aug. 1997.

[14]Barret, C., "Lifting Body Stability and Control," NASA TM-1999-209255, March 1999.

[15]Hollis, B. R., Thompson, R. A., Murphy, K. J., Nowak, R. J., Riley, C. J., Wood, W. A., Alter, S. J., and Prabhu, R. K., "X-33 Aerodynamic Computations and Comparisons with Wind-Tunnel Data," *Journal of Spacecraft and Rockets*, Vol. 38, No. 5, 2001, pp. 684–691.

[16]Murphy, K. J., Nowak, R. J., Thompson, R. A., Hollis, B. R., and Prabhu, R., "X-33 Hypersonic Aerodynamic Characteristics," *Journal of Spacecraft and Rockets*, Vol. 38, No. 5, 2001, pp. 670–683.

[17]Buck, G. M., "Automated Thermal Mapping Techniques Using Chromatic Image Analysis," NASA TM-101554, April 1989.

[18]Merski, N. R., "Reduction and Analysis of Phosphor Thermography Data with the IHEAT Software Package," AIAA Paper 98-0712, Jan. 1998.

[19]Merski, N. R., "Global Aeroheating Wind-Tunnel Measurements Using Improved Two-Color Phosphor Thermography Method," *Journal of Spacecraft and Rockets*, Vol. 36, No. 2, 1998, pp. 160–170.

[20]Buck, G. M., and Vasquez, P., "An Investment Ceramic Slip-Casting Technique for Net-Form, Precision, Detailed Casting of Ceramic Models," U. S. Patent 5,266,252, 30 Nov. 1993.

[21]Berry, S. A., Horvath, T. J., Kowalkowski, M. K., and Liechty, D. S., "X-33 (Rev-F) Aeroheating Results of Test 6770 in NASA Langley 20-Inch Mach 6 Air Tunnel," NASA TM-1999-209122, March 1999.

[22]Berry, S. A., Bouslog, S. A., Brauckmann, G. J., and Caram, J. M., "Shuttle Orbiter Experimental Boundary-Layer Transition Results with Isolated Roughness," *Journal of Spacecraft and Rockets*, Vol. 35, No. 3, 1998, pp. 241–248.

[23]Berry, S. A., Horvath, T. J., DiFulvio, M., Glass, C., and Merski, N. R., "X-34 Experimental Aeroheating at Mach 6 and 10," *Journal of Spacecraft and Rockets*, Vol. 36, No. 2, 1998, pp. 171–178.

[24]Horvath, T. J., Berry, S. A., Merski, N. R., and Fitzgerald, S. M., "X-38 Experimental Aerothermodynamics," AIAA Paper 2000-2685, June 2000.

[25]"GASP Version 3, The General Aerodynamic Simulation Program, Computational Flow Analysis Software for the Scientist and Engineer, User's Manual," AeroSoft, Inc., Blacksburg, VA, 1996.

[26]Olynick, D. R., and Tam, T., "Trajectory Based Validation of the Shuttle Heating Environment," *Journal of Spacecraft and Rockets*, Vol. 34, No. 2, 1997, pp. 172–181.

[27]Fay, J. A., and Riddell, F. R., "Theory of Stagnation Point Heat Transfer in Dissociated Air," *Journal of Aeronautical Sciences*, Vol. 25, No. 2, 1958, pp. 73–85.

[28]Bouslog, S. A., Moore, B., Lawson, I., and Sawyer, J. W., "X-33 Metallic Thermal Protection System Tests in NASA Langley Research Center High-Temperature Tunnel," AIAA Paper 99-1045, Jan. 1999.

[29]Palmer, G., Kontinos, D., and Sherman, B., "Surface Heating Effects of X-33 Vehicle Thermal Protection System Panel Bowing, Steps, and Gaps," AIAA Paper 98-0865, Jan. 1998.

[30]Horvath, T. J., Rhode, M. N., and Buck, G. M., "Aerothermodynamic Measurements on a Proposed Assured Crew Return Vehicle (ACRV) Lifting Body Configuration at Mach 6 and 10 in Air," AIAA Paper 90-1744, June 1990.

[31]Edney, B., "Anomalous Heat Transfer and Pressure Distributions on Blunt Bodies at Hypersonic Speeds in the Presence of an Impinging Shock," Aeronautical Research Inst. of Sweden, Rept. 115, Stockholm, Feb. 1968.

[32]Poll, D. I. A., "New Hypothesis for Transition on the Windward Face of the Space Shuttle," *Journal of Spacecraft and Rockets*, Vol. 23, No. 6, 1986, pp. 605–611.

T. C. Lin
Associate Editor

Color reproductions courtesy of NASA Langley Research Center.